Multi-scale modeling of the mechanical behavior of polycrystalline ice under transient creep.

Pierre Suquet, Hervé Moulinec, O. Castelnau, Maurine Montagnat, Noël Lahellec, Fanny Grennerat, Paul Duval, Renald Brenner

Multi-scale modeling of the mechanical behavior of polycrystalline ice under transient creep.

P. Suquet [1,2a], H. Moulinec[1,2], O. Castelnau[3], M. Montagnat[4], N. Lahellec[2,1] F. Grennerat[4] P. Duval,[4] R. Brenner[5]

[1] CNRS. LMA. UPR 7051. 13402. Marseille Cedex 20. France.
[2]Aix-Marseille Université. 60 rue Frédéric Joliot-Curie, 13453 Marseille Cedex 13, France.
[3]PIMM, CNRS, Arts & Métiers ParisTech, 151 Bd de l'hopital, 75013 Paris, France
[4]LGGE, UMR 5183, UJF-Grenoble1 / CNRS, 54 rue Molière, 38402 St Martin d'Hères, France
[5]LSPM. Université Paris 13 / CNRS. 99 av. J-B. Clément, 93430 Villetaneuse, France

Abstract

Ice is a challenging material for understanding the overall behavior of polycrystalline materials and more specifically the coupling between elastic and viscous effects during transient creep. At the single crystal level, ice is an hexagonal material with a rather weak elastic anisotropy but with a strong viscoplastic anisotropy. The strain-stress curve of ice single crystals shows a softening behavior depending on the strain-rate. The strong viscous anisotropy of ice gives rise to the progressive development of intergranular and intragranular strain heterogeneities and to stress concentrations which play an important role in the understanding of the creep behavior of ice polycrystals. The single crystal constitutive relations of Castelnau *et al* [1] are slightly modified here for a better evolution of the reference resolved shear stress on the slip systems and to account for kinematic hardening at the single crystal level. These constitutive relations are then used in a full-field simulation performed by an elasto-viscoplastic FFT-based method. The material parameters of the model are determined by comparison with experimental data available for single crystals as well as for polycrystals.

[a]suquet@lma.cnrs-mrs.fr

Keywords: polycrystal / ice / creep / elastoviscoplasticity / numerical homogenization / Fourier transform.

1 Introduction

This study is devoted to the multiscale modelling of transient creep of ice polycrystals. Transient creep is typically encountered when ice flow changes direction, such as in glaciers flowing above irregular bed rocks or submitted to tide forcing close to the sea-shore or in icy satellites. More generally, besides its intrinsic interest, understanding the transient creep response of ice gives insight in the elementary mechanisms taking place in polycrystalline materials and on their coupling. Compared to other materials with similar material properties (Mg alloys, for instance), ice is (relatively) easy to produce in the laboratory with a (rather) well-controlled microstructure. Also, by comparison with these other materials, experiments are (relatively) easier to perform (at least at high temperature, *i.e.* at about -10°). Therefore, besides its own interest, ice can be considered as a model material which can serve to assess the accuracy of constitutive models.

Significant progress has been made in the last two decades in the development of physically-based micromechanical models of polycrystalline materials, aiming at estimating their overall behavior from the knowledge of their microstructure (such as the lattice preferred orientation) and the elementary deformation mechanisms at the grain scale. However, the application of these models to geophysical materials has been limited so far to the prediction of either the purely elastic behavior or the purely viscoplastic behavior of polycrystals (see for instance Castelnau *et al* [2]). By contrast, the elasto-viscoplastic case has received much less attention.

The aim of this paper is two-fold. First, constitutive relations for ice single crystals matching available experimental data are presented in section 2. They are based on the constitutive relations proposed by Castelnau *et al* [1] with a few improvements consisting in a modification of the evolution law for the reference shear stress and the incorporation of a back-stress on each individual slip system. A partial identification of the material parameters entering the constitutive relations is performed in section 3 by comparison with experimental data for single crystals. However the material parameters pertaining to non-basal slip systems cannot be identified from single crystal data. Consequently, full-field simulations of polycrystalline aggregates

(where all slip systems are activated) are performed. The second objective of the present paper is to present the computational method used in these full-field simulations (section 4). The scheme is an extension to elasto-viscoplasticity of the FFT method originally proposed by Moulinec and Suquet [3]. Full-field simulations are used in section 5 to identify the material parameters which could not be identified from single crystal data. However it should be emphasized here that the interest of full-field simulations goes far beyond this identification. They have also been used in a separate paper for comparison of local strain fields with experimental data obtained by Digital Image Correlation (the interested reader is referred to Grennerat *et al* [4]). They have also been used as reference results to assess the accuracy of mean–field models for elasto-viscoplastic polycrystals (again not reported here, the interested reader is referred to Vu *et al* [5]).

2 Constitutive relations for ice single crystals

2.1 Experimental observations on ice single crystals and polycrystals

Ice is a strongly anisotropic hexagonal material that deforms plastically essentially by dislocation gliding on the basal plane (Duval [6]). There are three equivalent $<11\bar{2}0>$ directions for the Burgers vector and slip in the basal plane is almost isotropic. Since other slip systems are much stiffer than the basal ones, a single crystal oriented to favor basal slip deforms up to three orders of magnitude faster than a single crystal oriented to minimize the shear stress on the basal planes.

As for polycrystalline ice undergoing creep, the strain-rate drops by more than two orders of magnitude in the transient regime (Jacka [7] and figure 2) to reach a plateau in the secondary creep regime (which occurs at a strain of about 1%), following Andrade's law (Duval [8]). This decrease is associated with the development of large internal stress fields (Duval [6], Ashby and Duval [9], Castelnau *et al* [1]). A significant part of the transient creep is recoverable, i.e., on unloading a creep specimen, a reverse creep is observed, with reverse strain which can be more than ten times the initial elastic strain (Duval [8]). This reverse strain confirms the existence of strong directional internal stresses in polycrystals (by contrast with single crystals), due to plastic incompatibility between the grains. At the end of transient creep, a

regime of secondary creep is reached with a stress sensitivity exponent close to 3. Then, except at very low stress levels (below 0.1 MPa), tertiary creep associated with dynamic discontinuous recrystallization takes place with the generation of new grain microstructures and crystal orientations (Jacka and Maccagnan [10]). Tertiary creep will not be addressed here and secondary creep will be considered only as a limit case of transient creep which is the main objective of the present study.

2.2 Constitutive relations

The crystal plasticity model used at the single crystal level is based on the work of Castelnau *et al* [1], after a few modifications. As is usual in crystal plasticity, the viscoplastic strain results from slips on different slip systems:

$$\boldsymbol{\varepsilon} = \boldsymbol{\varepsilon}^{\mathsf{e}} + \boldsymbol{\varepsilon}^{\mathsf{vp}}, \quad \boldsymbol{\varepsilon}^{\mathsf{e}} = \boldsymbol{M}^{\mathsf{e}} : \boldsymbol{\sigma}, \quad \boldsymbol{\varepsilon}^{\mathsf{vp}} = \sum_{k=1}^{M} \gamma^{(k)} \boldsymbol{\mu}^{(k)}, \quad \boldsymbol{\mu}^{(k)} = \boldsymbol{m}^{(k)} \otimes_s \boldsymbol{n}^{(k)} \quad (1)$$

where M is the number of slip systems, $\boldsymbol{\mu}^{(k)}$ is the Schmid tensor of the k-th slip system with slip plane normal $\boldsymbol{n}^{(k)}$ and slip direction $\boldsymbol{m}^{(k)}$ (which is orthogonal to $\boldsymbol{n}^{(k)}$), and $\otimes_s$ indicates the (symmetrical) dyadic product.

Ice crystals, which have an hexagonal symmetry, deform easily by shear on the basal plane, on the three systems $\{0001\} < 11\bar{2}0 >$ which provide only two independent systems. The three prismatic systems $\{1\bar{1}00\} < 11\bar{2}0 >$ provide two more independent systems. An additional independent slip system is thus required to attain any isochoric deformation at the single crystal level and this is achieved by adding the six $< c + a >$ pyramidal systems $\{11\bar{2}2\} < 11\bar{2}\bar{3} >$. In total, $M = 12$ slip systems are taken into account in the present analysis.

In the constitutive relations originally proposed by Castelnau *et al* [1], the slip-rate on the k-th system is related to the resolved shear stress $\tau^{(k)}$ on that system through:

$$\dot{\gamma}^{(k)} = \dot{\gamma}_0^{(k)} \left(\frac{\left|\tau^{(k)}\right|}{\tau_0^{(k)}} \right)^{n^{(k)}} \operatorname{sgn}(\tau^{(k)}), \quad \tau^{(k)} = \boldsymbol{\sigma} : \boldsymbol{\mu}^{(k)}, \quad (2)$$

where $\tau_0^{(k)}$, the reference resolved shear stress on system k, depends on the

activity of the other systems through:

$$\dot{\tau}_0^{(k)} = \sum_{\ell=1}^{M} H^{(k,\ell)} \left(\frac{\tau_{sta}^{(\ell)} - \tau_0^{(\ell)}}{\tau_{sta}^{(\ell)} - \tau_{ini}^{(\ell)}} \right) \left| \dot{\gamma}^{(\ell)} \right| . \tag{3}$$

The two material parameters $\tau_{ini}^{(\ell)}$ and $\tau_{sta}^{(\ell)}$ refer respectively to the initial value of $\tau_0^{(\ell)}$ at the onset of plasticity (when the $\gamma^{(k)}$'s are small) and to the stationary value of $\tau_0^{(\ell)}$ at saturation (when the plasticity is fully developed, *i.e.* when the $\gamma^{(k)}$'s are large). Therefore the contribution of system ℓ in the hardening (or softening) of system k vanishes when $\tau_0^{(\ell)}$ is close to $\tau_{sta}^{(\ell)}$. The hardening matrix $H^{(k,\ell)}$ expresses the influence of the plastic activity of system ℓ on the hardening of system k and is taken to be symmetric. Material data for this model are given in Castelnau *et al* [1].

In the present study, the relations (2) and (3) are improved in two directions.

1. First kinematic hardening is introduced in (2) through a back-stress $X^{(k)}$:

$$\dot{\gamma}^{(k)} = \dot{\gamma}_0^{(k)} \left(\frac{\left| \tau^{(k)} - X^{(k)} \right|}{\tau_0^{(k)}} \right)^{n^{(k)}} \operatorname{sgn}\left(\tau^{(k)} - X^{(k)} \right), \tag{4}$$

   where the back-stress evolves with the plastic activity according to an Armstrong-Frederick type law including static recovery (Chaboche [11]) :

$$\dot{X}^{(k)} = c^{(k)} \dot{\gamma}^{(k)} - d^{(k)} X^{(k)} \left| \dot{\gamma}^{(k)} \right| - e^{(k)} \left| X^{(k)} \right|^{m} \operatorname{sign}\left(X^{(k)} \right). \tag{5}$$

   The introduction of a back-stress on each slip system is motivated by the experimental observation of recovery strain developing in single crystals when specimens are subjected to recovery mechanical tests (see section 3 and figure 1).

2. The equation governing the reference resolved shear stress $\tau_0^{(k)}$ is modified into

$$\dot{\tau}_0^{(k)} = \left(\tau_{sta}^{(k)} - \tau_0^{(k)} \right) \dot{p}^{(k)}, \quad \dot{p}^{(k)} = \sum_{\ell=1}^{M} h^{(k,\ell)} \left| \dot{\gamma}^{(\ell)} \right|, \tag{6}$$

   where the hardening matrix $h^{(k,l)}$ is different from $H^{(k,l)}$ but still symmetric (see table 1). The motivation for the change in the evolution

rule for the reference resolved shear stresses $\tau_0^{(k)}$ is that with the original rule (3) they never reach their stationary value, unless all systems do so at the same time, a condition which cannot be met in a polycrystal. Indeed, when the reference resolved shear stress $\tau_0^{(k)}$ on system k approaches $\tau_{sta}^{(k)}$, the self-hardening term in (3) vanishes, but if on another system ℓ the reference shear is not close to its stationary value, the latent hardening term proportional to $\tau_{sta}^{(\ell)} - \tau_0^{(\ell)}$ does not vanish, yielding a non-vanishing time derivative for $\tau_0^{(k)}$. Then $\tau_0^{(k)}$ can go beyond its stationary value and the sign of the self-hardening term changes, therefore leading to oscillations of $\tau_0^{(k)}$ which, as a consequence, never reaches a stationary plateau. By contrast, the law (6) ensures convergence of $\tau_0^{(k)}$ towards its stationary value, provided all coefficients $h^{(k,\ell)}$ are positive. Indeed, in this case, $\dot{p}^{(k)}$ is always positive and $p^{(k)}$ is increasing with time, playing on system k a role similar to the classical cumulated plastic strain of von Mises plasticity. The differential equation (6) can be integrated into

$$\tau_0^{(k)}(p^{(k)}) = \tau_{sta}^{(k)} + (\tau_{ini}^{(k)} - \tau_{sta}^{(k)})e^{(-p^{(k)})},$$

which shows that $\tau_0^{(k)} - \tau_{sta}^{(k)}$ has the same sign as $\tau_{ini}^{(k)} - \tau_{sta}^{(k)}$. Furthermore $\tau_0^{(k)}$ tends to $\tau_{sta}^{(k)}$ when $p^{(k)}$ becomes large.

The proposed constitutive relations can be formulated as a differential equation:

$$\dot{\boldsymbol{Y}} = \boldsymbol{F}(\dot{\boldsymbol{\varepsilon}}, \boldsymbol{Y}, t), \tag{7}$$

where

$$\boldsymbol{Y} = \begin{pmatrix} \boldsymbol{\sigma} \\ \tau_0^{(k)},\ k = 1, ...M \\ X^{(k)},\ k = 1, ...M \end{pmatrix}, \quad \boldsymbol{F}(\dot{\boldsymbol{\varepsilon}}, \boldsymbol{Y}, t) = \begin{pmatrix} \boldsymbol{L} : \left(\dot{\boldsymbol{\varepsilon}} - \sum_{k=1}^{M} \dot{\gamma}^{(k)}(\boldsymbol{Y}) \boldsymbol{\mu}^{(k)} \right) \\ \left(\tau_{sta}^{(k)} - \tau_0^{(k)} \right) \sum_{\ell=1}^{M} h^{(k,\ell)} \ \left| \dot{\gamma}^{(\ell)}(\boldsymbol{Y}) \right| \\ c^{(k)} \dot{\gamma}^{(k)}(\boldsymbol{Y}) - d^{(k)} X^{(k)} \left| \dot{\gamma}^{(k)}(\boldsymbol{Y}) \right| - e^{(k)} \left| X^{(k)} \right|^m \text{sign} \end{pmatrix} \tag{8}$$

with $\boldsymbol{L}$ the elastic stiffness and

$$\dot{\gamma}^{(k)}(\boldsymbol{Y}) = \dot{\gamma}_0^{(k)} \left(\frac{\left| \boldsymbol{\sigma} : \boldsymbol{\mu}^{(k)} - X^{(k)} \right|}{\tau_0^{(k)}} \right)^{n^{(k)}} \text{sign} \left(\boldsymbol{\sigma} : \boldsymbol{\mu}^{(k)} - X^{(k)} \right).$$

3 First identification of the constitutive relation

3.1 Elasticity

Ice crystals exhibit a weak elastic anisotropy, the Young's modulus varying by about 30% depending on the direction of loading with respect to the c-axis, the largest stiffness ($E \sim 11.8$GPa) being along the c-axis. The tensor of elastic moduli (in Kelvin's notations) at $-16°C$ reads as (Gammon [12]):

$$\begin{pmatrix} \sigma_{11} \\ \sigma_{22} \\ \sigma_{33} \\ \sqrt{2}\sigma_{23} \\ \sqrt{2}\sigma_{13} \\ \sqrt{2}\sigma_{12} \end{pmatrix} = \begin{pmatrix} 13930. & 7082. & 5765. & 0. & 0. & 0. \\ 7082. & 13930. & 5765. & 0. & 0. & 0. \\ 5765. & 5765. & 15010. & 0. & 0. & 0. \\ 0. & 0. & 0. & 6028. & 0. & 0. \\ 0. & 0. & 0. & 0. & 6028. & 0. \\ 0. & 0. & 0. & 0. & 0. & 6848. \end{pmatrix} \begin{pmatrix} \varepsilon^{\mathsf{e}}_{11} \\ \varepsilon^{\mathsf{e}}_{22} \\ \varepsilon^{\mathsf{e}}_{33} \\ \sqrt{2}\varepsilon^{\mathsf{e}}_{23} \\ \sqrt{2}\varepsilon^{\mathsf{e}}_{13} \\ \sqrt{2}\varepsilon^{\mathsf{e}}_{12} \end{pmatrix}$$

where all entries are in MPa and 3 is the axis of transverse isotropy (c-axis of the hexagonal crystalline structure).

3.2 Basal slip

The viscous and hardening properties of ice are strongly anisotropic. The identification of the different parameters of the model from available experimental data is radically different for basal systems and for non-basal systems. The literature provides a number of experimental data as for the behavior of ice crystals deformed in such a way that only basal slip is activated. However, due to the very large viscoplastic anisotropy of ice single crystals, mechanical tests have to be carried out very carefully to avoid any heterogeneity of the applied stress field.

Only the material parameters of (8) relevant for basal slip can be identified from experimental data on single crystals :

- First, data compiled by Duval [6] were used to determine the stationary flow stress and the stress sensitivity exponent $n^{(k)}$ of basal slip. There is quite a large spread in these experimental results from different authors, which can be attributed to several factors; for instance Chevy [13] has shown that the single crystal behavior can be significantly modified

by changing the surface roughness of the crystal. Despite these uncertainties, the stress sensitivity exponent for basal slip can be directly identified from these experimental data (numerical values are reported in Table 1), whereas the stationary flow stress depends on both the stationary reference stress $\tau_{sta}^{(k)}$ and the stationary backstress $X^{(k)}$.

- Next, data from Weertman [14] were used for the identification of the transient creep regime of basal systems. Single crystals were deformed under uniaxial compression at different strain-rates, with c-axis oriented at 45° from the loading direction (figure 1). The observed stress peak is associated with the increase in density of mobile dislocations (Duval [6]), a behavior typical for material with very low initial dislocation density (see *e.g.* Sauter and Leclercq [15], Cochard *et al* [16]). These tests shed light on the softening of basal slip in the transient regime. The static recovery term $e^{(k)}$ in the constitutive law (5) helps achieving the correct stationary stress at very small strain-rates (since $X^{(k)}$ tends to a constant value $c^{(k)}/d^{(k)}$ at large shear $\gamma^{(k)}$ if static recovery is not introduced).

- Finally, the recovery test of Taupin *et al* [17] performed on single crystals under uniaxial compression was considered. Here the c-axis orientation was not precisely defined experimentally, but it made an angle "less than 10°" with the compression direction. The single crystal was submitted to four creep loadings for 30 min separated by unloading stages for respectively 1 min, 10 min, and 100 min (figure 1 right). Upon reloading, the strain-rate is larger than just before the last unloading, indicating that dislocations are rearranging during the time intervals where the specimen is unloaded. This is accounted for in the model by the back stress $X^{(k)}$, and by $e^{(k)}$.

Figure 1 (left) shows the good match between the model (8) with the set of parameters given in Table 1 and these experimental results.

3.3 Non-basal systems

The authors are not aware of experiments performed on ice single crystals where only the non-basal systems are really activated. This would require straining the crystal along or perpendicular to the c-axis, but unfortunately

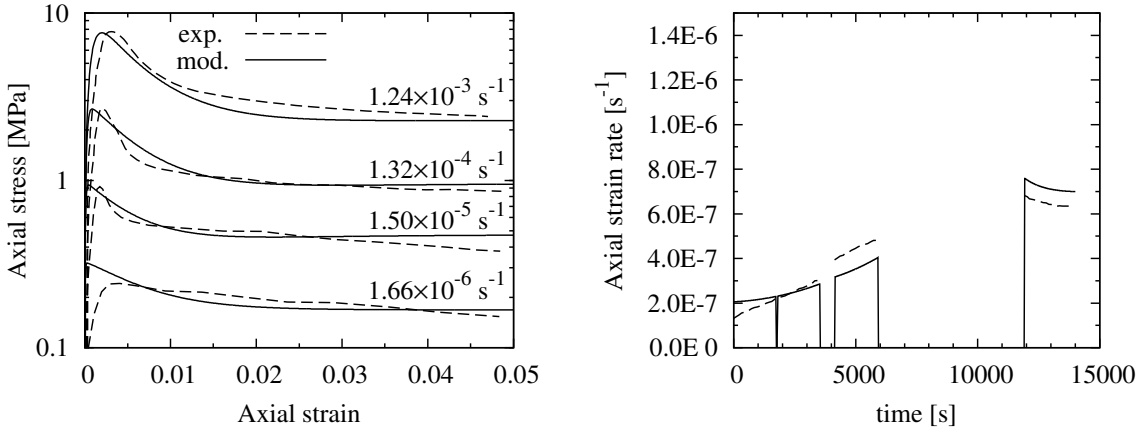

Figure 1: Behavior of ice single crystal deformed by basal slip. Left: comparison of the predictions of the model (8) with parameters given in Table 1 with the experimental data of Weertman [14]. Prescribed axial strain-rates are indicated. Right: comparison with the recovery test of Taupin *et al.* [17]. Temperature is $-10°$C.

any unavoidable deviation from perfect alignment activates basal slip. Duval [6] has given upper bounds for the flow stress on non-basal systems.

A first evaluation of the stress sensitivity exponents $n^{(k)}$ and stationary values $\tau_{sta}^{(k)}$ for prismatic and pyramidal systems can be found in Castelnau *et al* [18, 1]. In these two studies, use was made of the observed experimental responses of polycrystalline ice deformed under creep until the (stationary) secondary creep regime was reached. The overall specimen response was then modeled using two different extensions of the self-consistent scheme (the tangent linearization of Lebensohn and Tomé [19] and the affine linearization of Masson *et al* [20] respectively). Since only the secondary creep regime was of interest, the constitutive relation used in these mean-field simulation was purely viscoplastic and of the same form as equation (2), *i.e.* with no backstress $X^{(k)}$. The material parameters $n^{(k)}$ and $\tau_{sta}^{(k)}$ were then tuned to reproduce the overall response (stress sensitivity exponent and flow stress) of an untextured polycrystal and of several strongly anisotropic specimens from a Greenland ice core for which pronounced crystallographic textures have been measured and deformed under torsion and compression along different directions (Castelnau *et al* [2]).

In the present study, the stress sensitivity exponents $n^{(k)}$ found by Castelnau *et al* [1] were used, whereas the stationary reference stresses were slightly tuned. The other non-basal parameters which were left undetermined by these previous studies (initial reference stresses, hardening parameters), were identified by trial-and-error by comparing full-field simulations with the experimental data compiled by Ashby and Duval [9] for the transient creep response of untextured (isotropic) polycrystals. This identification requires the development of the constitutive relations (8) in a full-field code. This implementation is described in the next section.

4 Implementation of crystalline elastoviscoplastic laws in a FFT code

4.1 Local problem

We consider a polycrystalline volume V composed of several grains of different orientations, each grain obeying the constitutive relations (8). The volume V is subjected to a macroscopic loading path, which can be a prescribed history of averaged strain, or a history of averaged stress or a combination of both. For simplicity, it is assumed here that the loading consists of a prescribed history of macroscopic strain $\overline{\boldsymbol{\varepsilon}}(t), t \in [0,T]$. Other types of loadings can be handled by different methods described in Michel *et al* [21] for instance.

The local problem to be solved to determine the local stress and strain fields in the volume element V consists of the equilibrium equations, compatibility conditions, constitutive relations and periodicity boundary conditions:

$$\left.\begin{array}{lll} (\dot{\boldsymbol{\sigma}}, \dot{\boldsymbol{\tau}}_0, \dot{\boldsymbol{X}}) = \boldsymbol{F}(\dot{\boldsymbol{\varepsilon}}, \boldsymbol{\sigma}, \boldsymbol{\tau}_0, \boldsymbol{X}, \boldsymbol{x}, t), & & \text{for } (\boldsymbol{x},t) \in V \times [0,T], \\ \boldsymbol{\varepsilon}(\boldsymbol{x},t) = \frac{1}{2}(\nabla \boldsymbol{u}(\boldsymbol{x},t) + {}^{\mathsf{T}}\nabla \boldsymbol{u}(\boldsymbol{x},t)), & \text{div } \boldsymbol{\sigma}(\boldsymbol{x},t) = 0 & \text{for } (\boldsymbol{x},t) \in V \times [0,T], \\ \boldsymbol{u}(\boldsymbol{x},t) - \overline{\boldsymbol{\varepsilon}}(t).\boldsymbol{x} \text{ periodic on } \partial V, & & \text{for } t \in [0,T] \end{array}\right\} \tag{9}$$

We are interested both in the effective response $\overline{\boldsymbol{\sigma}}(t),\ t \in [0,T]$ of the composite to the history of the averaged strain $\overline{\boldsymbol{\varepsilon}}(t),\ t \in [0,T]$, but also in the local fields $\boldsymbol{\sigma}(\boldsymbol{x},t), \boldsymbol{\varepsilon}(\boldsymbol{x},t)$ and other significant fields (internal variables thermodynamic forces etc....).

The numerical method used to solve the local problem (9) is based on

Fast Fourier Transforms (more specifically on Discrete Fourier Transforms). Initially proposed by Moulinec and Suquet [22, 3] for N-phase composites with complex microstructure, the method has been extended to viscoplastic polycrystals by Lebensohn [23] and to shape memory polycrystals (in a model situation of antiplane shear) by Bhattacharaya and Suquet [24]. An extension of the method to elastoviscoplastic composites (with isotropic phases) was briefly outlined in Idiart *et al* [25] and used to discuss the intra-phase field fluctuations in two-phase composites. The FFT method is gaining popularity for simulating the response of volume elements of heterogeneous materials under periodic boundary conditions (these boundary conditions are essential to allow for the use of the FFT). A non-exhaustive list of contributions using or improving on the initial method includes Muller [26], Eyre and Milton [27], Michel *et al* [21, 28], Brown *et al* [29], Bonnet [30], Vinogradov and Milton [31], Nguyen *et al* [32], Brisard and Dormieux [33], Zeman *et al* [34], Belkhabbaz *et al* [35] among others.

An extension of the simplest version of the FFT-based method, often called the *basic scheme*, to constitutive relations including crystalline elasto-viscoplasticity is proposed here. It relies on two ingredients:

1. *A time-integration scheme for the constitutive differential equations.* The time interval of interest $[0, T]$ is split into time steps $[t_n, t_{n+1}]$. All quantities are assumed to be known at time t_n. The quantities at time t_{n+1} are unknown. This time integration is performed at every point $\boldsymbol{x}$ separately and the evolution problem is reduced to a problem for the stress and strain fields $\boldsymbol{\sigma}$ and $\boldsymbol{\varepsilon}$ at time t_{n+1} in the form
$$\boldsymbol{\sigma}_{n+1}(\boldsymbol{x}) = \boldsymbol{\mathcal{F}_{n+1}}(\boldsymbol{x}, \boldsymbol{\varepsilon}_{n+1}(\boldsymbol{x})). \tag{10}$$
2. *A FFT global scheme to solve a local problem for a nonlinear composite obeying (10).*

4.2 A class of constitutive relations

The algorithm which we have used applies to a wide class of constitutive relations which we now briefly describe.

1. First these constitutive relations require state variables of the problem to be identified. These state variables include the strain $\boldsymbol{\varepsilon}$ and additional *internal variables* $\boldsymbol{\alpha}$ from which the stress $\boldsymbol{\sigma}$ can be expressed:
$$\boldsymbol{\sigma} = \boldsymbol{\mathcal{L}}(\boldsymbol{\varepsilon}, \boldsymbol{\alpha}). \tag{11}$$

In the present example of crystalline elastoviscoplasticity, the internal variables are the slips on the different slip systems

$$\boldsymbol{\alpha} = \left\{ \gamma^{(k)}, k = 1, .., M \right\}, \tag{12}$$

and the relation (11) is provided by the first equation in (8). Additional internal variables (such as the $p^{(k)}$'s) could be added to the list of internal variables for the purpose of post-processing the results.

2. The change in the internal variables at time t depends on the value at time t of the stress $\boldsymbol{\sigma}$ and of *thermodynamic forces* $\boldsymbol{\mathcal{A}}$:

$$\dot{\boldsymbol{\alpha}} = \boldsymbol{\mathcal{H}}(\boldsymbol{\sigma}, \boldsymbol{\mathcal{A}}). \tag{13}$$

In the present model of crystalline elastoviscoplasticity the thermodynamic forces are the reference stress and the back-stress on each slip system:

$$\boldsymbol{\mathcal{A}} = \left\{ \tau_0^{(k)}, X^{(k)}, k = 1, .., M \right\}. \tag{14}$$

3. The change in the thermodynamic forces depends on the stress $\boldsymbol{\sigma}$ and on the change in the internal variables:

$$\dot{\boldsymbol{\mathcal{A}}} = \boldsymbol{\mathcal{G}}(\boldsymbol{\sigma}, \dot{\boldsymbol{\alpha}}). \tag{15}$$

In the present model of crystalline elastoviscoplasticity this evolution equation corresponds to the two last equations in (8).

Taking the time derivative of equation (11) and using equation (13) gives:

$$\dot{\boldsymbol{\sigma}} = \frac{\partial \boldsymbol{\mathcal{L}}}{\partial \boldsymbol{\varepsilon}} : \dot{\boldsymbol{\varepsilon}} + \frac{\partial \boldsymbol{\mathcal{L}}}{\partial \boldsymbol{\alpha}} : \boldsymbol{\mathcal{H}}(\boldsymbol{\sigma}, \boldsymbol{\mathcal{A}}) = \boldsymbol{F}_{\sigma}(\dot{\boldsymbol{\varepsilon}}, \boldsymbol{\sigma}, \boldsymbol{\mathcal{A}}).$$

Similarly using (13) in (15), one obtains an evolution equation for $\boldsymbol{\sigma}$ and $\boldsymbol{\mathcal{A}}$ in the form:

$$\dot{\boldsymbol{\mathcal{A}}} = \boldsymbol{F}_{\mathcal{A}}(\boldsymbol{\sigma}, \boldsymbol{\mathcal{H}}(\boldsymbol{\sigma}, \boldsymbol{\mathcal{A}})).$$

Finally, the constitutive relations take the form of a differential equation for $\boldsymbol{\sigma}$ and $\boldsymbol{\mathcal{A}}$:

$$\dot{\boldsymbol{Y}} = \boldsymbol{F}(\dot{\boldsymbol{\varepsilon}}, \boldsymbol{Y}), \quad \text{where} \quad \boldsymbol{Y} = (\boldsymbol{\sigma}, \boldsymbol{\mathcal{A}}) \tag{16}$$

In the present model of crystalline elastoviscoplasticity, these equations correspond to (8).

4.3 Time-integration of the constitutive relations

The differential equation (16) can be integrated in time at every point $\boldsymbol{x}$ of the representative volume element. In the rest of this subsection, the material point $\boldsymbol{x}$ is fixed and the dependence on $\boldsymbol{x}$ of all fields is omitted for simplicity.

The evolution problem is discretized in time, *i.e.* the time interval $[0, T]$ of interest is subdivided into subintervals $[t_n, t_{n+1}]$. Knowing all fields of interest at time t_n $(\boldsymbol{\varepsilon}_n, \boldsymbol{\sigma}_n, \boldsymbol{\mathcal{A}}_n)$, where the subscript n refers to time t_n, the unknowns are the same quantities $(\boldsymbol{\varepsilon}_{n+1}, \boldsymbol{\sigma}_{n+1}, \boldsymbol{\mathcal{A}}_{n+1})$ at time t_{n+1}.

Assume for a moment that $\boldsymbol{\varepsilon}_{n+1}$ is known. Then the strain-rate $\dot{\boldsymbol{\varepsilon}}$ can be approximated by

$$\dot{\boldsymbol{\varepsilon}} \simeq \frac{\boldsymbol{\varepsilon}_{n+1} - \boldsymbol{\varepsilon}_n}{t_{n+1} - t_n},$$

and the differential equation (16) can be integrated in time on the interval $[t_n, t_{n+1}]$. Numerous schemes are available to perform this time-integration which, roughly speaking, can be classified into two main categories, explicit shemes on one hand and implicit schemes on the other hand. As is well-known the main advantage of the explicit schemes is their simplicity and their main drawback is their conditional convergence (at least for methods without adaptative stepping). The main advantage of implicit methods is their stability and consistency, which allows for large time-steps, whereas their main disadvantage is the fact that they require solving a nonlinear problem which comes at a high cost. As is well known (see for instance Chaboche and Cailletaud [36], Saleeb *et al* [37] among many others), implicit schemes are often preferable when the FEM is chosen to solve the global problem (equilibrium + compatibility), as their stability allows for larger time-steps. However the FFT method, at least in its most basic version, requires rather small time-steps for convergence to be reached in only a few iterations. Therefore explicit schemes compare favorably with implicit schemes in the context of the FFT basic algorithm.

The results presented here were obtained with an explicit Runge-Kutta (RK) scheme with adaptative time-stepping (Runge-Kutta of order 4(3) using local extrapolation and FSAL, see A), which achieves a good compromise between simplicity and efficiency. The method does not require solving a nonlinear problem and no gradient of $\boldsymbol{F}$ has to be computed. The outcome of the time-integration is the updated set of forces $(\boldsymbol{\sigma}_{n+1}, \boldsymbol{\mathcal{A}}_{n+1})$. Since $\boldsymbol{\varepsilon}_{n+1}$ was assumed to be known at the beginning of this resolution, $(\boldsymbol{\sigma}_{n+1}, \boldsymbol{\mathcal{A}}_{n+1})$ are functions of $\boldsymbol{\varepsilon}_{n+1}$, even though these functions cannot be explicited in

closed form. In summary, at each material point $\boldsymbol{x}$ of the representative volume element, the time-integration of the constitutive relations provides a nonlinear relation between $\boldsymbol{\varepsilon}_{n+1}$ and $\boldsymbol{\sigma}_{n+1}$ which we can write formally in the form (10).

4.4 FFT algorithm

We now turn to the resolution of the boundary value problem on a volume element V composed of several different phases or grains, each of them obeying a constitutive law in the form (16). After time-integration the constitutive relations in (9) are reduced to (10). The local problem to solved at times t_{n+1} therefore reads as (the subscript $n+1$ is omitted to simplify notations, $\boldsymbol{\sigma}$ and $\boldsymbol{\varepsilon}$ stand for $\boldsymbol{\sigma}_{n+1}$ and $\boldsymbol{\varepsilon}_{n+1}$):

$$\left.\begin{array}{c} \boldsymbol{\sigma}(\boldsymbol{x}) = \boldsymbol{\mathcal{F}}(\boldsymbol{x}, \boldsymbol{\varepsilon}(\boldsymbol{x})), \quad \boldsymbol{\varepsilon}(\boldsymbol{x}) = \frac{1}{2}(\nabla \boldsymbol{u}(\boldsymbol{x}) + {}^{\mathsf{T}}\nabla \boldsymbol{u}(\boldsymbol{x})), \quad \text{div } \boldsymbol{\sigma}(\boldsymbol{x}) = 0 \quad \text{for } \boldsymbol{x} \in V, \\ \boldsymbol{u}(\boldsymbol{x}) - \overline{\boldsymbol{\varepsilon}}.\boldsymbol{x} \text{ periodic on } \partial V. \end{array}\right\} \tag{17}$$

A linear, homogeneous, material with stiffness $\boldsymbol{L}^{(0)}$ is introduced and, following Moulinec and Suquet [3], the nonlinear constitutive relations are rewritten as :

$$\boldsymbol{\sigma}(\boldsymbol{x}) = \boldsymbol{L}^{(0)} : \boldsymbol{\varepsilon}(\boldsymbol{x}) + \boldsymbol{\tau}(\boldsymbol{x}), \quad \boldsymbol{\tau}(\boldsymbol{x}) = \boldsymbol{\mathcal{F}}(\boldsymbol{x}, \boldsymbol{\varepsilon}(\boldsymbol{x})) - \boldsymbol{L}^{(0)} : \boldsymbol{\varepsilon}(\boldsymbol{x}).$$

The solution to the thermoelastic problem

$$\left.\begin{array}{c} \boldsymbol{\sigma}(\boldsymbol{x}) = \boldsymbol{L}^{(0)} : \boldsymbol{\varepsilon}(\boldsymbol{x}) + \boldsymbol{\tau}(\boldsymbol{x}), \quad \boldsymbol{\varepsilon}(\boldsymbol{x}) = \frac{1}{2}(\nabla \boldsymbol{u}(\boldsymbol{x}) + {}^{\mathsf{T}}\nabla \boldsymbol{u}(\boldsymbol{x})), \quad \text{div } \boldsymbol{\sigma}(\boldsymbol{x}) = 0 \quad \text{for } \boldsymbol{x} \in V, \\ \boldsymbol{u}(\boldsymbol{x}) - \overline{\boldsymbol{\varepsilon}}.\boldsymbol{x} \text{ periodic on } \partial V. \end{array}\right\} \tag{18}$$

is known and writes in real space and Fourier space respectively ($\boldsymbol{\xi}$ denotes the frequency in Fourier space and the Fourier transform of a function $f(\boldsymbol{x})$ is denoted as $\hat{f}(\boldsymbol{\xi})$):

$$\boldsymbol{\varepsilon}(\boldsymbol{u}(\boldsymbol{x})) = \overline{\boldsymbol{\varepsilon}} - \boldsymbol{\Gamma}^0 * \boldsymbol{\tau}(\boldsymbol{x}), \quad \hat{\boldsymbol{\varepsilon}}(\boldsymbol{\xi}) = -\hat{\boldsymbol{\Gamma}}^0(\boldsymbol{\xi}) : \hat{\boldsymbol{\tau}}(\boldsymbol{\xi}), \quad \hat{\boldsymbol{\varepsilon}}(\boldsymbol{0}) = \overline{\boldsymbol{\varepsilon}}, \tag{19}$$

where $*$ denotes convolution in real space. $\boldsymbol{\Gamma}^0$ is the Green operator associated with the linear elastic reference medium whose Fourier transform $\hat{\boldsymbol{\Gamma}}^0$ is explicitely known (Moulinec and Suquet [3]). Substituting the expression of $\boldsymbol{\tau}$ in (19) leads to the nonlinear Lippman-Schwinger equation

$$\boldsymbol{\varepsilon} = \overline{\boldsymbol{\varepsilon}} - \boldsymbol{\Gamma}^0 * \left(\boldsymbol{\mathcal{F}}(\boldsymbol{\varepsilon}) - \boldsymbol{L}^{(0)} : \boldsymbol{\varepsilon}\right). \tag{20}$$

This equation is solved by a fixed point algorithm:

$$\boldsymbol{\varepsilon}^{(k+1)} = \overline{\boldsymbol{\varepsilon}} - \boldsymbol{\Gamma}^0 * \left(\boldsymbol{\mathcal{F}}(\boldsymbol{\varepsilon}^{(k)}) - \boldsymbol{L}^{(0)} : \boldsymbol{\varepsilon}^{(k)} \right), \tag{21}$$

where the superscript k is relative to the k-th iteration. The following property of the Green's operator $\boldsymbol{\Gamma}^{(0)}$ can be used to simplify further the algorithm, for any compatible field $\boldsymbol{\varepsilon}$ with average $\overline{\boldsymbol{\varepsilon}}$ one has ([28]):

$$\boldsymbol{\Gamma}^0 * \boldsymbol{L}^{(0)} : \boldsymbol{\varepsilon} = \boldsymbol{\varepsilon} - \overline{\boldsymbol{\varepsilon}}.$$

The Lippman-Schwinger equation then takes the simpler form:

$$\boldsymbol{\varepsilon}^{(k+1)} = \boldsymbol{\varepsilon}^{(k)} - \boldsymbol{\Gamma}^0 * \boldsymbol{\sigma}^{(k)}, \quad \text{where} \quad \boldsymbol{\sigma}^{(k)} = \boldsymbol{\mathcal{F}}(\boldsymbol{\varepsilon}^{(k)}). \tag{22}$$

The algorithm can be summarized as follows:

Initialize:

- $\boldsymbol{\varepsilon}^{(k=0)}(\boldsymbol{x})$ *is initialized (see below)*
- $\boldsymbol{\sigma}^{(k=0)}(\boldsymbol{x}) = \boldsymbol{\mathcal{F}}(\boldsymbol{\varepsilon}^{(k=0)}(\boldsymbol{x}))$. *Note that* $\boldsymbol{\mathcal{F}}$ *depends on* $\boldsymbol{\varepsilon}_n(\boldsymbol{x})$, $\boldsymbol{\sigma}_n(\boldsymbol{x})$ *and* $\boldsymbol{\mathcal{A}}_n(\boldsymbol{x})$.

repeat

The fields $\boldsymbol{\varepsilon}^{(k)}$ and $\boldsymbol{\sigma}^{(k)}$ being known:
(1) Take the Fourier transform of the stress field:
$\hat{\boldsymbol{\sigma}}^{(k)} = FFT(\boldsymbol{\sigma}^{(k)})$,
(2) Check equilibrium in Fourier space.
(3) Update the strain field in Fourier space:

$$\hat{\boldsymbol{\varepsilon}}^{(k+1)}(\boldsymbol{\xi}) = \hat{\boldsymbol{\varepsilon}}^{(k)}(\boldsymbol{\xi}) - \hat{\boldsymbol{\Gamma}}^0(\boldsymbol{\xi}) : \hat{\boldsymbol{\sigma}}^{(k)}(\boldsymbol{\xi}) \quad \forall \boldsymbol{\xi} \neq \mathbf{0} \text{ and } \hat{\boldsymbol{\varepsilon}}^{(k+1)}(0) = \overline{\boldsymbol{\varepsilon}}, \tag{23}$$

(4) Take the inverse Fourier transform of the updated strain field:
$\boldsymbol{\varepsilon}^{(k+1)}(\boldsymbol{x}) = FFT^{-1}(\hat{\boldsymbol{\varepsilon}}^{(k+1)}(\boldsymbol{\xi}))$
(5) Apply the constitutive relations in real space:
$\boldsymbol{\sigma}^{(k+1)}(\boldsymbol{x}) = \boldsymbol{\mathcal{F}}(\boldsymbol{\varepsilon}^{(k+1)}(\boldsymbol{x}))$.

until *convergence reached*;

FFT and FFT^{-1} stand for the (fast and discrete) Fourier transform and its inverse.

Initialization step At the beginning of a time-step, the strain field can be initialized according to two slightly different procedures. For general

loadings, the simplest initialization reads as:

$$\boldsymbol{\varepsilon}^{(k=0)}(\boldsymbol{x}) = \boldsymbol{\varepsilon}_n(\boldsymbol{x}) + \overline{\boldsymbol{\varepsilon}}_{n+1} - \overline{\boldsymbol{\varepsilon}}_n \quad \forall\ \boldsymbol{x} \in\ V.$$

However, for monotone and radial loadings the algorithm can be accelerated by extrapolating the initial strain field from the two preceeding time steps:

$$\boldsymbol{\varepsilon}^{(k=0)}(\boldsymbol{x}) = \boldsymbol{\varepsilon}_n(\boldsymbol{x}) + \frac{t_{n+1} - t_n}{t_n - t_{n-1}}(\boldsymbol{\varepsilon}_n(\boldsymbol{x}) - \boldsymbol{\varepsilon}_{n-1}(\boldsymbol{x})) \quad \forall\ \boldsymbol{x} \in\ V.$$

The latter initialization procedures requires to store the strain field at the two previous time-steps.

Stress control The above algorithm assumes that the overall strain applied to the polycrystal is controlled (the history $\overline{\boldsymbol{\varepsilon}}(t)$ is prescribed). However many applications correspond to a stress-controlled situation (where the history $\overline{\boldsymbol{\sigma}}(t)$ is prescribed). This is in particular the case of creep tests which are used to calibrate the material parameters of the model.

The control of the overall stress requires a modification of step 3 in the above strain-controlled algorithm. The last item of equation (23) is replaced by

$$\hat{\boldsymbol{\varepsilon}}^{(k+1)}(0) = \overline{\boldsymbol{\varepsilon}}^{k+1}, \quad \text{with} \quad \overline{\boldsymbol{\varepsilon}}^{(k+1)} = \overline{\boldsymbol{\varepsilon}}^{(k)} + \left(\boldsymbol{L}^{(0)}\right)^{-1} : (\overline{\boldsymbol{\sigma}} - \hat{\boldsymbol{\sigma}}^{(k)}(\mathbf{0})), \quad (24)$$

where $\overline{\boldsymbol{\sigma}}$ is the "target" stress and where $\hat{\boldsymbol{\sigma}}^{(k)}(\mathbf{0}) = \left\langle \boldsymbol{\sigma}^{(k)} \right\rangle$.

Convergence test (step (2)) In the strain-controlled method the criterion for convergence consists in checking equilibrium.

$$\left\| \mathrm{div}(\boldsymbol{\sigma}^{(k)}) \right\|_2 \leq \mathrm{tol}_1 \left| \overline{\boldsymbol{\sigma}}^{(k)} \right|, \quad (25)$$

where $\|.\|_2$ denotes the L^2 norm and $|.|$ is is the euclidian norm of a second-order tensor. Plancherel's theorem, according to which the L^2 norm of a function in real space coincides with the L^2 norm of its Fourier transform in Fourier space, can be used to express the convergence criterion (25) in Fourier space as:

$$\left\| \boldsymbol{\xi}.\hat{\boldsymbol{\sigma}}^{(k)}(\boldsymbol{\xi}) \right\|_2 \leq \mathrm{tol}_1 \left| \hat{\boldsymbol{\sigma}}^{(k)}(\mathbf{0}) \right|, \quad (26)$$

In the stress controlled approach, in addition to equilibrium, a second test is required to check that the condition on the overall stress is met:

$$|\hat{\boldsymbol{\sigma}}^{(k)}(\mathbf{0}) - \overline{\boldsymbol{\sigma}}| \leq \text{tol}_2 \; |\overline{\boldsymbol{\sigma}}|. \tag{27}$$

The results presented in the next section were obtained with:

$$\text{tol}_1 = 10^{-3}, \; \text{tol}_2 = 10^{-4}$$

.

Rate of convergence of the iterative algorithm The choice of the reference medium has a strong influence on the convergence rate of the method (see Michel *et al*, 2001, for more details). The choice of the elastic stiffness $\boldsymbol{L}^{(0)}$ is inspired from a (rigorous) choice in the case of a N phase composite with isotropic phases, where the optimal $\boldsymbol{L}^{(0)}$ is an isotropic tensor with Lamé coefficient $\lambda^{(0)}$ set to $\frac{1}{2}(\lambda_{max}+\lambda_{min})$ (similar expression for $\mu^{(0)}$), where λ_{max} and λ_{min} are the largest and smallest Lamé coefficients of the phases. This recipe is applied to polycrystals by bounding from above and below the elastic stiffness of the single crystal by two isotropic tensors and by taking the mid-value of the Lame coefficients of these two bounds.

There is no proof that this choice is optimal in the transient elasto-viscoplastic regime, but a convergence in a few iterations was observed with this choice, provided that the time steps were small enough, a constraint which is imposed anyway to achieve convergence of the RK4 scheme.

5 Final calibration of the model

The material parameters of the constitutive model described in equation (7) are fine-tuned by performing several full-field simulations of the creep experiments compiled by Ashby and Duval [9]. These simulations were performed on 3D artificial microstructures obtained by Voronoi tesselation and consisting of 4096 cells (or grains). The corresponding microstructures were discretized into images containing $256 \times 256 \times 256$ voxels (figure 2 left).

The creep conditions which were considered consist in the application at $t = 0$ of an axial stress $\overline{\sigma}_{33}$ (all other components of the overall stress vanishing). This axial stress is applied to the polycrystal and kept constant for about 48h. Therefore the time interval of interest (in seconds) is from

$t = 0s$ to $t = 120000s$. This time interval is discretized in 10679 time steps of unequal sizes (the time-steps being smaller at the beginning of the loading, when the convergence of the iterative process is more difficult to achieve, and then increased). Each simulation performed with Craft (FFT-based program developed at the CNRS/LMA, freely available at `http://craft.lma.cnrs-mrs.fr`) took 92 hours on a 8 cores Xeon W5580 workstation (CPU clock 3.2GHz) and several simulations were run with different sets of material parameters.

After several trials and errors we arrived at the set of material parameters given in table 1. These parameters are not claimed to be optimal but, at least, the predictions obtained with these parameters compare well with the experimental data as shown in figure 1 for single crystals tests and in figure 2 for creep experiments on polycrystals.

Strain fields observed experimentally using Digital Image Correlation on two-dimensional polycrystals (columnar grains) and full-field simulations were also found to be in good qualitative agreement. These results are reported in a companion paper (Grennerat *et al* [4]).

6 Concluding remarks

A constitutive model for ice single crystals has been proposed. The corresponding material parameters have been identified by comparison with experimental data available in the literature for single crystals as well as for polycrystals. This constitutive model has been implemented in a code based on Fast Fourier Transforms. Its predictions for the global response of polycrystalline aggregates under transient creep are in good agreement with experiments available in the literature as well as with new experiments carried out in the course of this study (Grennerat [4]). Full-field simulations could also be useful in two directions: a detailed comparison of the statistics of the local strain fields (*e.g.* first and second moments) within each individual grains and an assessment of the accuracy of micromechanical schemes for the overall properties of elasto-viscoplastic polycrystals. These directions are currently being investigated (Vu *et al* [5]).

Acknowledgments This study was funded by the French 'Agence Nationale de la Recherche' (project ELVIS, #ANR-08-BLAN-0138).

	τ_{ini}	τ_{sta}	$\dot{\gamma}_0$	n	c	d	e	m
Basal	0.1	0.022	10^{-6}	2	9	60	0.0003	1
Prismatic	0.13	1.5	10^{-6}	2.85	9	60	0.0003	1
Pyramidal	3.875	3.875	10^{-6}	4	9	60	0.0003	1

(28)

Hardening matrix:

	Basal	Prismatic	Pyramidal
Basal	70	125	0
Prismatic	125	110	0
Pyramidal	0	0	0

(29)

Table 1: Material parameters used in the full-field simulations for single crystals of ice at $-10°C$. Units are MPa and s^{-1}.

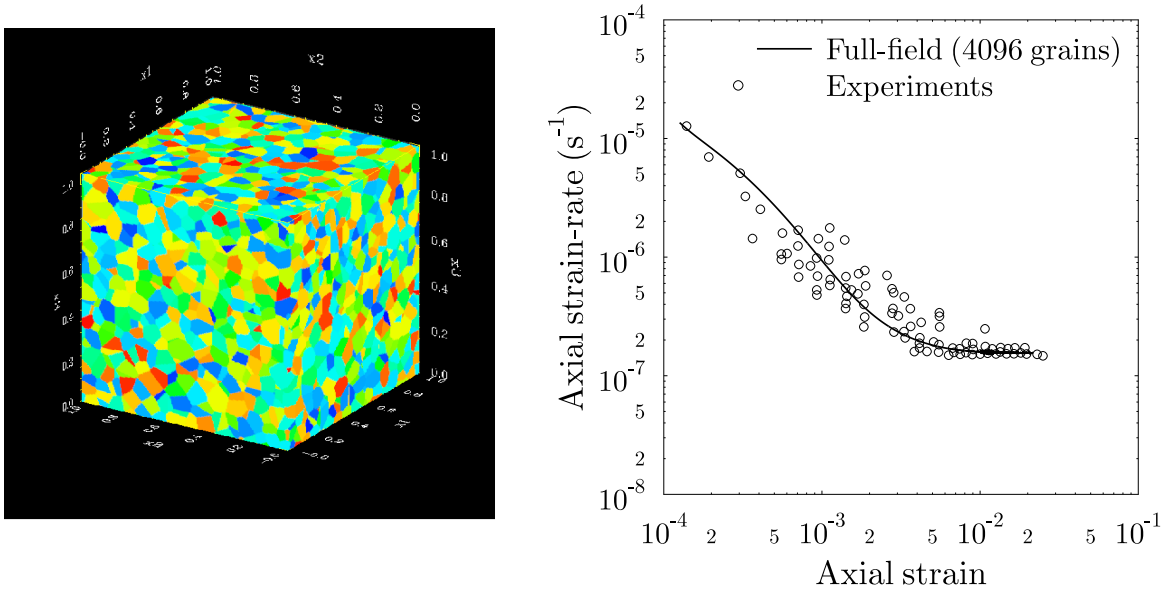

Figure 2: Transient creep experiments. Comparison between the experimental results compiled by Ashby and Duval [9] and the full-field simulations performed on the configuration on the left with the FFT solver, the crystalline model (8) and material data given in table 1.

References

[1] O. Castelnau, P. Duval, M. Montagnat, R. Brenner, Elastoviscoplastic micromechanical modeling of the transient creep of ice, J. Geophysical Research **113** (2008) B11203.

[2] O. Castelnau, H. Shoji, A. Mangeney, H. Misch, P. Duval, A. Miyamoto, K. Kuwabara, O. Watanabe, Anisotropic behavior of GRIP ices and flow in central Greenland, Earth Planet. Sci. Lett. **160** (1998) 1–13.

[3] H. Moulinec, P. Suquet, A numerical method for computing the overall response of nonlinear composites with complex microstructure, Comp. Meth. Appl. Mech. Engng. **157** (1998) 69–94.

[4] F. Grennerat, M. Montagnat, O. Castelnau, P. Vacher, H. Moulinec, P. Suquet, P. Duval, Intragranular strain field in columnar ice during transient creep, Acta Mater. , submitted.

[5] Q. H. Vu, R. Brenner, O. Castelnau, H. Moulinec, P. Suquet, A self-consistent estimate for linear viscoelastic polycrystals with internal variables inferred from the collocation method, Modelling and Simulation in Materials Science and Engineering , submitted.

[6] P. Duval, M. Ashby, I. Anderman, Rate controlling processes in the creep of polycrystalline ice, J. Phys. Chem. **87** (1983) 4066–4074.

[7] T. Jacka, The time and strain required for development of minimum strain rates in ice, Cold Reg. Sc. Technol. **8** (1984) 261–268.

[8] P. Duval, Anelastic behaviour of polycrystalline ice, J. Glaciol. **21** (1978) 621–628.

[9] M. Ashby, P. Duval, The creep of polycrystalline ice, Cold Reg. Sci. Technol. **11** (1985) 285–300.

[10] T. Jacka, M. Maccagnan, Ice crystallographic and strain rate changes with strain in compression and extension, Cold Reg. Sc. Technol. **8** (1984) 269–286.

[11] J. Chaboche, A review of some plasticity and viscoplasticity constitutive theories, Int. J. Plasticity **24** (2008) 1642–1693.

[12] P. H. Gammon, H. Kiefte, M. J. Clouter, W. W. Denner, Elastic constants of artificial and natural ice samples by Brillouin spectroscopy, J. Glaciol. **29** (1983) 433–460.

[13] J. Chevy, Viscoplasticité et hétérogénéités de déformation du monocristal de glace : expériences et simulations, Ph.D. thesis, Université Joseph Fourier (Grenoble, France) (2008).

[14] J. Weertman, Creep of ice, in: E. Whalley, S. Jones, L. Gold (Eds.), Physics and Chemistry of Ice, Roy. Soc. Canada, Ottawa, 1973, pp. 320–337.

[15] J. Sauter, S. Leclercq, Modeling of the non-monotonous viscoplastic behavior of uranium dioxide, J. Nucl. Mater. **322** (2003) 1–14.

[16] J. Cochard, I. Yonenaga, S. Gouttebroze, M. M'Hamdi, Z. L. Zhang, Constitutive modeling of intrinsic silicon monocrystals in easy glide, J. Appl. Phys. **107** (2010) 033512–033520.

[17] V. Taupin, T. Richeton, J. Chevy, C. Fressengeas, J. Weiss, F. Louchet, M. Miguel, Rearrangement of dislocation structures in the aging of ice single crystals, Acta Mater. **56** (2008) 1555–1563.

[18] O. Castelnau, G. Canova, R. Lebensohn, P. Duval, Modelling viscoplastic behavior of anisotropic polycrystalline ice with a self-consistent approach, Acta Mater. **45** (1997) 4823–4834.

[19] R. Lebensohn, C. Tomé, A self-consistent anisotropic approach for the simulation of plastic deformation and texture development of polycrystals: Application to zirconium alloys, Acta Materiala **41** (1993) 2611–2624.

[20] R. Masson, M. Bornert, P. Suquet, Z. A., An affine formulation for the prediction of the effective properties of nonlinear composites and polycrystals, J. Mech. Phys. Solids **48** (2000) 1203–1227.

[21] J. Michel, H. Moulinec, P. Suquet, Effective properties of composite materials with periodic microstructure: a computational approach, Comp. Meth. Appl. Mech. Engng. **172** (1999) 109–143.

[22] H. Moulinec, P. Suquet, A fast numerical method for computing the linear and nonlinear properties of composites, C. R. Acad. Sc. Paris II **318** (1994) 1417–1423.

[23] R. Lebensohn, N-site modelling of a 3d viscoplastic polycrystal using Fast Fourier Transforms, Acta Materiala **49** (2001) 2723–2737.

[24] K. Bhattacharya, P. Suquet, A model problem concerning recoverable strains of shape-memory polycrystals, Proc. R. Soc. London A **461** (2005) 2797–2816.

[25] M. Idiart, H. Moulinec, P. Ponte Castañeda, P. Suquet, Macroscopic behavior and field fluctuations in viscoplastic composites: second-order estimates versus full-field simulations, J. Mech. Phys. Solids **54** (2006) 1029–1063.

[26] W. Müller, Mathematical versus experimental stress analysis of inhomogeneities in solids, J. Physique IV **6** (1996) C1.139–C1–148.

[27] D. Eyre, G. Milton, A fast numerical scheme for computing the response of composites using grid refinement, J. Physique III **6** (1999) 41–47.

[28] J. Michel, H. Moulinec, P. Suquet, A computational method for linear and nonlinear composites with arbitrary phase contrast, Int. J. Numer. Meth. Engng **52** (2001) 139–160.

[29] C. Brown, W. Dreyer, W. Müller, Discrete Fourier transforms and their application to stress-strain problems in composite mechanics: A convergence study, Proc. R. Soc. London A **458** (2002) 1–21.

[30] G. Bonnet, Effective properties of elastic periodic composite media with fibers, J. Mech. Phys. Solids **55** (2007) 881–899.

[31] V. Vinogradov, G. Milton, An accelerated FFT algorithm for thermoelastic and nonlinear composites, International Journal for Numerical Methods in Engineering **76** (2008) 1678–1695.

[32] T.-K. Nguyen, K. Sab, G. Bonnet, Green's operator for a periodic medium with traction-free boundary conditions and computation of the effective properties of thin plates, Int. J. Solids Struct. **45** (2008) 6518–6534.

[33] S. Brisard, L. Dormieux, FFT-based methods for the mechanics of composites: A general variational framework, Computational Materials Science **49** (2010) 663 – 671.

[34] J. Zeman, J. Vondřejc, J. Novák, I. Marek, Accelerating a FFT-based solver for numerical homogenization of periodic media by conjugate gradients, Journal of Computational Physics **229** (2010) 8065–8071.

[35] A. Belkhabbaz, R. Brenner, N. Rupin, B. Bacroix, J. Fonseca, Prediction of the overall behavior of a 3d microstructure of austenitic steel by using FFT numerical scheme, Procedia Engineering **10** (2011) 1883–1888.

[36] J. Chaboche, G. Cailletaud, Integration methods for complex plastic constitutive equations, Comput. Methods Appl. Mech. Engrg **133** (1996) 125–155.

[37] A. Saleeb, T. Wilt, W. Li, Robust integration schemes for generalized viscoplasticity with internal-state variables, Computers and Structures **74** (2000) 601–628.

[38] M. Sofroniou, G. Spaletta, Construction of explicit Runge-Kutta pairs with stiffness detection, Mathematical and Computer Modelling **40** (2004) 1157–1169.

A Two classical time-integration schemes

The differential system to be integrated reads as:

$$\dot{\boldsymbol{Y}} = \boldsymbol{F}(t, \boldsymbol{Y}(t)), \quad \boldsymbol{f} : \mathbb{R}^{N+1} \longrightarrow \mathbb{R}^N, \quad \boldsymbol{Y}(t=0) = \boldsymbol{Y}_0. \tag{30}$$

Among many possibilities, two integration schemes are very commonly used for the integration of (30).

A.1 Runge-Kutta scheme of order p with prescribed time-stepping: RKp

In a Runge-Kutta scheme of order p with prescribed time-steps, the solution of (30) is approximated as:

$$\boldsymbol{Y}_{n+1} = \boldsymbol{Y}_n + \sum_{j=1}^{p} c_j \ \boldsymbol{K}_j, \tag{31}$$

with

$$\left\{\begin{array}{lcl} \boldsymbol{K}_1 &=& h\ \boldsymbol{F}(t_n, \boldsymbol{Y}_n) \\ \boldsymbol{K}_2 &=& h\ f\boldsymbol{F}(t_n + a_2\ h,\ \boldsymbol{Y}_n + b_{21}\ \boldsymbol{K}_1) \\ \ldots & & \\ \boldsymbol{K}_p &=& h\ \boldsymbol{F}((t_n + a_s\ h,\ \boldsymbol{Y}_n + \sum_{j=1}^{p-1} b_{pj}\ \boldsymbol{K}_j) \end{array}\right.$$

The coefficients $\{a_i,\ b_{ij},\ c_i\}_{i=1,p;j=1,i}$ are chosen such that the above approximation $\boldsymbol{Y}_{n+1}$ coincides with the exact solution $\boldsymbol{Y}(t_{n+1})$, up to order p. These coefficients are given in the form of a table (Butcher table) whose general form is given in (32) left, and which takes the particular form on the right of (32) for the standard Runge-Kutta method of order 4 (RK4) :

$$\begin{array}{c|ccccc} 0 & 0 & 0 & & & \\ a_2 & b_{21} & 0 & & & \\ a_3 & b_{31} & b_{32} & 0 & & \\ . & . & . & . & & \\ a_p & b_{p1} & b_{p2} & \ldots & b_{p,p-1} & 0 \\ \hline & c_1 & c_2 & \ldots & c_{p-1} & c_p \end{array} \qquad \begin{array}{c|cccc} 0 & 0 & 0 & & \\ 1/2 & 1/2 & 0 & & \\ 1/2 & 0 & 1/2 & 0 & \\ 1 & 0 & 0 & 1 & 0 \\ \hline & 1/6 & 1/3 & 1/3 & 1/6 \end{array} \qquad (32)$$

In the case of the RK4 scheme, the approximation (31) becomes:

$$\boldsymbol{Y}_{n+1} = \boldsymbol{Y}_n + \frac{h}{6}\left(\boldsymbol{K}_1 + 2\boldsymbol{K}_2 + 2\boldsymbol{K}_3 + \boldsymbol{K}_4\right), \quad h = t_{n+1} - t_n \qquad (33)$$

where

$$\boldsymbol{K}_1 = h\,\boldsymbol{F}(t_n, \boldsymbol{Y}_n), \quad \boldsymbol{K}_2 = h\,\boldsymbol{F}(t_n + \frac{h}{2},\ \boldsymbol{Y}_n + \frac{h}{2}\boldsymbol{K}_1), \quad \boldsymbol{K}_3 = h\,\boldsymbol{F}(t_n + \frac{h}{2},\ \boldsymbol{Y}_n + \frac{h}{2}\boldsymbol{K}_2), \quad \boldsymbol{K}_4 = h\,\boldsymbol{F}($$

A.2 Runge-Kutta scheme with adaptative time-stepping RK$p(p-1)$

Generally speaking, a time integration with adaptative time-stepping requires two main ingredients:

1. A method for estimating the error which is made at each time step.

2. A method for controlling and adapting the time-step.

The error is estimated by means of the *local extrapolation method*. Two different solutions are evaluated with two schemes of order p and $p-1$ respectively (hence the denomination RK$p(p-1)$):

$$\left\{ \begin{array}{rcl} \boldsymbol{Y}_{n+1} & = & \boldsymbol{Y}_n + \sum_{j=1}^{p} c_j \ \boldsymbol{K}_j, \quad \text{RK of order } p \\ \boldsymbol{Y}^*_{n+1} & = & \boldsymbol{Y}_n + \sum_{j=1}^{p} c^*_j \ \boldsymbol{K}_j, \quad \text{RK of order } p-1. \end{array} \right. \tag{34}$$

Note that the two evaluations make use of the same values $\{\boldsymbol{K}_i\}_{i=1,p}$ of the function $\boldsymbol{F}$. The solution at order p, which is the most accurate, is chosen as reference. The local absolute errors is defined as

$$err_{n+1} = \boldsymbol{Y}_{n+1} - \boldsymbol{Y}^*_{n+1} = \sum_{j=1}^{p} \left(c_j - c^*_j\right) \ \boldsymbol{K}_j,$$

whereas the relative error is defined as:

$$||\delta_{n+1}|| = max_i(\delta^{(i)}_{n+1}), \quad \text{where} \quad \delta^{(i)}_{n+1} = \frac{\left| Y^{(i)}_{n+1} - Y^{(i)\ *}_{n+1} \right|}{t_a + t_r \ \left| \boldsymbol{Y}^{(i)}_{n+1} \right|} \tag{35}$$

(in our implementation, $t_a = 10^{-10}$ and $t_r = 1$).

Since the most precise Runge-Kutta scheme used in (34) is of order p, the error δ for a time step h goes as h^p. Assume that a guess h_n for the n-th time step has been made leading to a relative error $||\delta_n||$ according to (35). For a given tolerance Tol on the error, the appropriate length of the n-th time step should be :

$$h_n \left(\frac{Tol}{||\delta_n||} \right)^{\frac{1}{p}}, \ \text{where } h_n = t_n - t_{n-1}. \tag{36}$$

If the error is less than the tolerance, *i.e.* $||\delta_n|| \leq Tol$, the current n-th time step is accepted and the size h_{n+1} of the further time step is initialized by (36). Otherwise, if the error is larger than the tolerance, *i.e.* $||\delta_n|| > Tol$, the current step is rejected and the step size h_n is reduced according to (36).

In practice, the time step adaptation differs slightly from (36) and follows the "Proportional-Integral Step Control" which smoothens the variations of

the time step as:

$$h_n \; s_1 \; \left(\frac{s_2 \; Tol}{||\delta_n||} \right)^{\frac{k_1}{p}} \left(\frac{||\delta_{n-1}||}{||\delta_n||} \right)^{\frac{k_2}{p}}, \tag{37}$$

with the following parameters in our implementation: $k_1 = 1, \;\; k_2 = 0$ and $s_1 = \frac{17}{20}, \;\; s_2 = \frac{9}{10}$.

Finally, a variant of the method, known as the FSAL (First Same As Last), is used in the present study. It is such that the last evaluation of $\boldsymbol{F}$ at a given time step coincides with the first evaluation of $\boldsymbol{F}$ at the new time step. This implies sevarl relations between the coefficients entering the Butcher table. The Butcher table for the the RK-FSAL scheme of order 4(3) reads as (Sofroniou and Spaletta [38]):

$$\begin{array}{c|ccccc}
0 & 0 & & & & \\
2/5 & 2/5 & 0 & & & \\
3/5 & -3/20 & 3/4 & 0 & & \\
1 & 19/44 & -15/44 & 10/11 & 0 & \\
1 & 11/72 & 25/72 & 25/72 & 11/72 & 0 \\
\hline
c_i & 11/72 & 25/72 & 25/72 & 11/72 & 0 \\
\hline
c_i - c_i^* & \frac{119041}{8970912} & -\frac{595205}{8970912} & \frac{595205}{8970912} & \frac{1309451}{8970912} & -\frac{119041}{747576}
\end{array} \tag{38}$$